Investigating lubricant behavior in a partially flooded tapered roller bearing: Validation of a multiphase CFD solver for aerated oil sump via

Citation for the original published paper (version of record):
Maccioni, L., Chernoray, V., Concli, F. (2025). Investigating lubricant behavior in a partially flooded tapered roller bearing: Validation of a
multiphase CFD solver for aerated oil sump via particle image velocimetry studies and
high-speed camera acquisitions. Tribology International, 201.
http://dx.doi.org/10.1016/j.triboint.2024.110274

Tribology International 201 (2025) 110274

Contents lists available at ScienceDirect

Tribology International

journal homepage: www.elsevier.com/locate/triboint

Investigating lubricant behavior in a partially flooded tapered roller bearing: Validation of a multiphase CFD solver for aerated oil sump via particle image velocimetry studies and high-speed camera acquisitions

Lorenzo Maccioni [a,*], Valery G. Chernoray [b], Franco Concli [a]

[a] Free University of Bozen-Bolzano, Faculty of Engineering, Piazza Università 1, 39100, Bolzano, Italy
[b] Chalmers University of Technology, Mechanics and Maritime Sciences, 41259 Gothenburg, Sweden

ARTICLE INFO

Keywords:
Tapered roller bearing
Lubrication
PIV
Aeration
Partially flooded

ABSTRACT

In the recent years, the efficacy of utilizing sapphire outer rings as a viable tool for experimentally observing oil flows within rolling bearings has been demonstrated. However, in previous studies, such approach was applied under fully-flooded lubrication conditions exclusively. This paper presents the outcomes of observations and measurements conducted under oil-bath lubrication conditions of a vertical-axis Tapered Roller Bearing (TRB). The experimental work encompasses four operational speeds ranging from 1000 min^{-1} to 2500 min^{-1}, and two oil levels, i.e. 10% and 100% of the bearing width. Pictures were captured using an High-Speed Camera (HSC) for a qualitative inspection. Particle Image Velocimetry (PIV) measurements were conducted for a quantitative assessment of the oil velocity fields. The findings reveal specific lubricant flows, highlight aeration, and show particular vorticity patterns that intensify with increasing speed. These experimentally obtained results align with Computational Fluid Dynamics (CFD) simulations conducted using a specially developed model in OpenFOAM®, leveraging a solver that accounts for aeration.

1. Introduction

Studying the lubricant behavior within rolling element bearings, both experimentally and numerically, is a flourishing research topic [1,2]. Recent experimental studies have employed optical methods, such as High-Speed Imaging (HSI) or Particle Image Velocimetry (PIV) measurements, to both qualitatively and quantitatively assess the lubricant distribution and/or its velocity field under specific lubrication regimes and conditions. Moreover, the temperatures distribution and then the effectiveness of lubrication in specific areas of rolling bearings have been studied, recently, using thermal cameras [3–6].

HSI has been utilized to qualitatively evaluate the dynamic of lubricants near bearings, as reported in [7–9]. Studies involving both experimental observations and numerical simulations by Wen et al. [8] and Santhosh et al. [9] have elucidated the splash behavior of ball bearings encased in various cages, identifying distinct splash patterns attributable to different cage designs through macroscopic observations (possible thanks to transparent surfaces). Furthermore, Wu et al. [7] conducted an experimental campaign to examine flow patterns and thermal characteristics in jet-lubricated ball bearings, employing an axial viewpoint for image capturing that revealed a concentration of oil near the nozzles, aiding in the optimal placement and quantity of nozzles for effective lubrication. Similarly, Santhosh et al. [9] employed an axial perspective to probe the mechanisms of oil dispersion near an aero-engine ball bearing, identifying three distinct oil fragmentation processes across varying velocity spectrums — ranging from direct droplet formation at lower velocities to ligament fragmentation and sheet disintegration at higher velocities.

The experimental setup initially designed by Russell et al. [10] for investigating the frictional dynamics between the ball and cage of a deep groove ball bearing was modified by Aamer et al. [11] for optical measurements. This apparatus was engineered to precisely regulate the rotational velocity of a 12 mm-diameter ball within a segment of a full-sized bearing, excluding the outer ring. It facilitated the adjustment of the cage's position relative to the spinning ball by measuring the torque exerted on the ball. In this particular study, the cage was constructed from acrylic to ensure transparency and was kept stationary relatively to the absolute frame of reference, thus enabling a clear observation of the space between the cage and the ball. The absence of the outer ring was deliberate to permit unobstructed optical access. Measurements were conducted at various ball speeds (up to 1200 min^{-1}) and cage-ball relative position. The findings were then juxtaposed with outcomes derived from multiphase CFD simulations,

* Corresponding author.
E-mail address: lorenzo.maccioni@unibz.it (L. Maccioni).

https://doi.org/10.1016/j.triboint.2024.110274
Received 13 July 2024; Received in revised form 10 September 2024; Accepted 20 September 2024
Available online 25 September 2024

showcasing a notable correlation and underscoring the significant role of surface tension in influencing lubricant distribution patterns. Aamer et al. [11] also noted an increase in air entrapment within the cage-ball interface as the gap narrowed. Furthermore, an increase in ball velocity led to a proliferation of finer lubricant streaks on the ball's surface. However, the investigation did not extend to the effects of real motion forces exerted by the ball, cage, and inner ring, nor did it consider the outer ring's impact. The focus remained solely on mapping the flow distribution, omitting velocity analyses.

In their innovative researches, Chen et al. [12,13] delve into the challenging task of quantifying the actual volume of lubricating oil within the contact regions of a real ball bearings having 18 balls and a diameter of inner raceway of 45.8 mm. Employing a pioneering experimental setup that merges synchronized dual-camera imaging with Laser-Induced Fluorescence (LIF) and additional illumination, they provided a detailed visualization of oil flow dynamics within a ball bearing. The main findings revealed the majority of the oil layer on component surfaces does not actively participate in the lubrication of contact areas. Notably, as the rolling contact traverses, the thinning of the oil layer exposes areas of decay, critically impairing the process of oil replenishment, a phenomenon that intensifies with higher capillary numbers. To facilitate these observations and ensure clear visibility of the oil surrounding the outer contacts, balls, and cage pockets, the cage and outer ring materials were manufactured from transparent resin and glass. The research encompasses tests conducted up to 5000 min^{-1}, utilizing both radial and axial cameras to capture the oil behavior.

The study conducted by Fan et al. [14] outlines the development of a specialized rolling bearing test rig designed to emulate the multi-faceted contacts of rolling bearings, diverging from the simpler ball-on-disc models to provide a more realistic analysis of lubrication dynamics. Utilizing a deep groove ball bearing with a transparent glass outer ring and fluorescent dye-tagged oil, the study employs LIF to map out the three-dimensional oil distribution across a range of rotational speeds up to 1000 min^{-1}. The findings reveal the formation of distinct, independent oil pools at lower speeds, which merge into interconnected oil strings as the speed increases. The study delves into how variations in oil supply and rotational speed influence the distribution of these oil reservoirs, noting the expansion of the oil string and reservoir width with increased speed. Moreover, it highlights the occurrence of cavitation, which affects the continuity of the oil supply to the bearing contacts.

In [11], the research delves into the complex dynamics of lubrication within a ball bearing cage. A novel test setup featuring a transparent cage, mirroring the original cage geometry, enabled direct observation of lubricant and air entrapment under various operational scenarios, utilizing a High-Speed Camera (HSC). Findings indicate significant changes in lubrication conditions and increased air entrapment as the cage approached closer to the ball. The study underscored the crucial influence of lubricant surface tension on the formation of striation patterns across the ball's surface.

The study presented in [15] delves into the phenomenon of oil starvation across various cage designs in horizontally mounted ball bearings, employing a counter-rotating angular contact ball bearing test rig to capture the oil distribution within transparent cages, manufactured in acrylic, through HSI. The research explored the impact of cage geometry, oil viscosity, and operational dynamics on lubrication effectiveness, revealing that factors such as the motion of the raceway, the degree of ball immersion, and the properties of the oil significantly affect the lubrication within the cage pockets, evidenced by the formation of oil–air striations on the ball surface.

Noda et al. [16,17] utilized X-ray computed tomography to visualize the distribution of grease within ball bearings. Due to the limitations imposed by the high X-ray intensities required for imaging metal components, which hinder the resolution needed for detailed grease mapping, the researchers opted for a fluoro-resin carbon fiber composite to construct the inner and outer rings as well as the cage, with the balls manufactured from glass. This approach enabled the utilization of the technology up to a shaft speed of 600 min^{-1}, the maximum permitted by the system's frequency capture capability. The findings from these experiments indicate that grease tends to accumulate in specific areas of the bearing at such speeds. Additionally, the study facilitated the observation of grease transitioning from a circulating to a channeling state, attributed to the varying X-ray absorption properties of mixed urea and barium-based greases. In [18], utilizing optical methods that combine a HSC with a microscope, starvation and replenishment of grease near the contact area in a thrust bearing have been studied. The authors highlighted significant differences between the results obtained from the ball-on-disc configuration and those observed in a real thrust bearing.

In [19], the lubricant film thickness in a Tapered Roller Bearing (TRB), more specifically a SKF 81208TN, has been estimated exploiting Electrical Impedance Spectroscopy (EIS). The scholars, tracking the bearing's resistance and capacitance using EIS across different rotational speeds (up to 1400 min^{-1}) noted a shift from boundary to mixed lubrication, as well as the subsequent transition from mixed lubrication to EHL.

Regarding studies involving PIV measures, Gorse et al. [20] investigated the formation of droplets within the chambers of aero-engine bearings utilizing PIV techniques. A specialized test apparatus was devised to reproduce realistic conditions for a cylindrical roller bearing. Through axial imaging, the process of capturing and processing images highlighted the significant role that bearing support plays in the creation of droplets.

Yan et al. [21] conducted PIV analysis within the space of an angular contact ball bearing to examine predominant air flows and vortex patterns. For the PIV studies from a radial angle, key elements such as the cage, the outer ring, and the bearing's exterior were manufactured from Perspex facilitating visual access to the bearing's interior. Utilizing HSC images and cross-correlation analysis, the research team was able to map out the velocity field across a radial section of the bearing. This approach unveiled distinct vortices adjacent to the rolling elements, with their intensity found to increase with the bearing's rotational velocity. Nevertheless, the mechanical properties of Perspex limited the maximum achievable rotational speed at 1300 min^{-1}.

Moreover, [22] extends the investigation performed in [15] to the dynamics of oil flows in angular contact ball bearings using Bubble Image Velocimetry (BIV), a technique derived from PIV that employs bubbles as tracers to assess flow velocity. This approach, facilitated by a similar counter-rotating rig, allowed for the observation of oil distribution at various speeds and cage configurations, ensuring optimal oil levels within the bearing. Various cage designs were evaluated at inner ring rotational speeds reaching 400 min^{-1} to prevent oil leakage. The study by [22], employing BIV, suggests that rolling element bearings are prone to air bubble entrapment within the lubricating oil, particularly under oil bath lubrication conditions. This phenomenon, known as aeration [23,24], occurs when the oil fails to release the trapped air over extended periods, potentially leading to the formation of foaming. Aeration and foaming negatively affect the properties of the lubricant, leading to reduced heat removal efficiency by the fluid, lower thermal capacity, decreased viscosity, increased corrosiveness, higher susceptibility to cavitation, and reduced filterability [25]. In [26], a method for experimentally studying the dynamics of aeration and de-aeration in terms of volume fraction and bubble size was presented. Additionally, in [26–28], the mechanisms and effects of anti-foaming agents that reduce the presence of foam and aeration are discussed; these additives primarily function by lowering the surface tension at the oil–air interface.

However, the aforementioned studies exclusively apply either HSI or PIV techniques to ball bearings. The only research involving the use of PIV measurements on TRBs has been conducted by Maccioni et al. in [29–31]. In the latter works, utilizing a sapphire-made outer ring, the scholars achieved clear optical insight into the TRB's internal

dynamics. The PIV studies allowed to map the lubricant's velocity patterns within the space separating the outer ring and the cage across a spectrum of rotational speeds, reaching up to 2500 min^{-1} of the inner ring. This area is notably critical for observing the pumping effect, as highlighted in [32]. Throughout their experiments, Maccioni et al. [29,30] noted the emergence of bubbles with increased rotational speeds, indicative of aeration, mirroring foaming behaviors observed in earlier research by Liebrecht et al. [33,34]. This phenomenon was also observed with an oil level that covered the TRB by as much as 3 times its width (considering a vertical-axis TRB). Therefore, to conduct measurements under fully-flooded lubrication conditions without air bubble interference, the test rig was enhanced and a different type of oil was used in the experiments conducted in [31]. This adjustment enabled the study of oil flows in the absence of aeration. As a result, it was observed that edge effects at the ends of the rollers could be significant. It was also noted that the flow velocity between the cage and the outer ring can exceed that of the cage itself. Furthermore, with an increase in rotational speed, the maximum flow velocity shifts away from the roller pushing the lubricant and moves towards the roller that draws in the fluid due to suction [31].

The article [35] presents an exclusively numerical analysis of oil lubrication and cooling in a TRB, specifically the SKF 29460E, used in a high-performance mixed-flow pump. The study employs ANSYS CFX to simulate the oil–air multiphase flow within the bearing, incorporating thermal effects (with an estimated 5 kW of load-dependent power losses at 276 min^{-1}) and an unsteady flow model using a transient solver through the multiple reference frame approach. The analysis revealed load-independent power losses within the bearing amounting to 3 kW and provided insights into the effectiveness of the oil bath lubrication method with partially submerged rollers. However, this study was experimentally validated only through temperature measurements, with no flow data being monitored. Another paper that applies CFD to TRB is [36]. In this study, a two-row TRB with different rib structures was analyzed under loss of lube conditions. The CFD study was performed using a multiphase turbulent model with a multiple reference frame approach. However, no experimental validations were conducted to verify the results.

Based on the available evidence, it can be asserted that TRBs have been primarily investigated under fully-flooded lubrication conditions, both with and without aerated oil, employing PIV techniques (or were not validated through any optical methods). While these conditions hold academic significance, they do not represent the most common lubrication practices. Indeed, TRBs are more frequently lubricated using oil-bath methods with partial filling in real-world settings. This article aims to present the findings of an experimental campaign that examined oil flows in a TRB under partial oil bath lubrication conditions. The study explores the lubricant dynamics both quantitatively, using PIV measurements, and qualitatively, through HSI, offering insights into the behavior of lubrication practices more closely aligned with industrial usage. Furthermore, from a numerical perspective, there is a clear need to validate multiphase CFD solvers that account for aeration in lubrication, as this phenomenon is frequently encountered in real-world systems. This article presents and discusses the development of a solver capable of considering oil aeration, along with its application under oil-bath lubrication conditions in a TRB.

2. Experimental approaches

2.1. Test rig and oil properties

The test rig employed in this research is also described in [29–31]. The geometry of the TRB 32312-A, manufactured by Schaeffler Technologies AG & Co, was studied. The geometric specifications of this TRB are detailed in Table 1. A key feature of the test rig is the outer ring made of sapphire, which, due to its transparency, allows for a radial optical access inside the TRB; permitting PIV and HSI tests.

Table 1
Dimensions of 32312-A bearing.

Symbol	Description	Value	Unit
d	Bore diameter	60	mm
D	Outside diameter	130	mm
B	Total Width	48.5	mm
n	Number of rollers	16	–
D_p	Pitch diameter	94.8	mm
d_R	Mean roller diameter	17.4	mm
ϕ	Angle of contact	11	°

To enhance surface clarity, grinding and polishing operations were performed, ensuring that the geometry of the outer ring meets the geometric and dimensional tolerances of the original steel design. The hardness of sapphire is sufficient to prevent scratches or wear on the inner race, maintaining its optical properties throughout the test. This enables the TRB to be loaded with the minimum load required to ensure the correct kinematics of the rollers, specifically a no-slip condition. The original metallic rollers, cage, and inner ring were used in this study.

Fig. 1 illustrates the test rig in its assembled state along with its CAD model. The working principle of the test rig involves the control of axial loading of the bearing via a central screw located at the bottom of the rig. This screw deforms the cup springs, generating an axial force that is conveyed to the outer ring and transmitted to the frame through the screw. This axial force, which can reach up to 5 kN, is transferred from the outer ring through the rollers to the inner ring, shaft, angular contact bearing, and ultimately to the frame.

After preloading the system to ensure the correct kinematics of the components, the shaft can be rotated using a three-phase 2.2 kW electric motor with velocity feedback, controlled by an inverter and coupled to the shaft through a bellows joint.

For this study, two different oil levels have been applied: 10% and 100% of the bearing width. These two oil levels can be considered as low (10%) and high (100%). In both cases, the proportion is straightforward to set experimentally, ensuring the repeatability of the tests. The rotation of the TRB components induces a pumping effect, as schematically shown in the CAD model in Fig. 1, which highlights the primary oil paths with yellow arrows. The vertical architecture of the test rig ensures axis-symmetrical operating conditions for lubricant distribution, with gravity acting parallel to the axis of rotation. Fig. 1 also depicts two chambers containing the lubricant: the lower and upper chambers relative to the TRB. Oil temperature in each chamber was monitored using thermocouples. Additionally, six O-rings, visible in Fig. 1, prevent oil leakage. Dampers were incorporated to minimize vibrations at the base of the test rig. During operation under oil-bath lubrication, HSI and PIV measurements can be performed through a designated window that allows optical access, as shown in Fig. 1.

The oil utilized in this experimental campaign is Castrol Syntrans 75W-85, with properties detailed in Table 2. The table includes the fitting parameters (A, B) of the Andrade Equation (Eq. (1)), which can be used to estimate the dynamic viscosity (μ) as a function of temperature (ϑ). Parameters B and A are determined according to Eqs. (2) and (3), respectively. The relationship between dynamic viscosity (μ) and kinematic viscosity (ν) is defined by Eq. (4).

$$\mu(\vartheta) = Ae^{B/\vartheta} \tag{1}$$

$$B = -ln\left(\frac{\mu_{40\ °C}/\mu_{100\ °C}}{40\ °C - 100\ °C}\right) \tag{2}$$

$$A = \mu_{100\ °C} \cdot e^{B\cdot(100+273)} \tag{3}$$

$$\nu = \frac{\mu}{\rho} \tag{4}$$

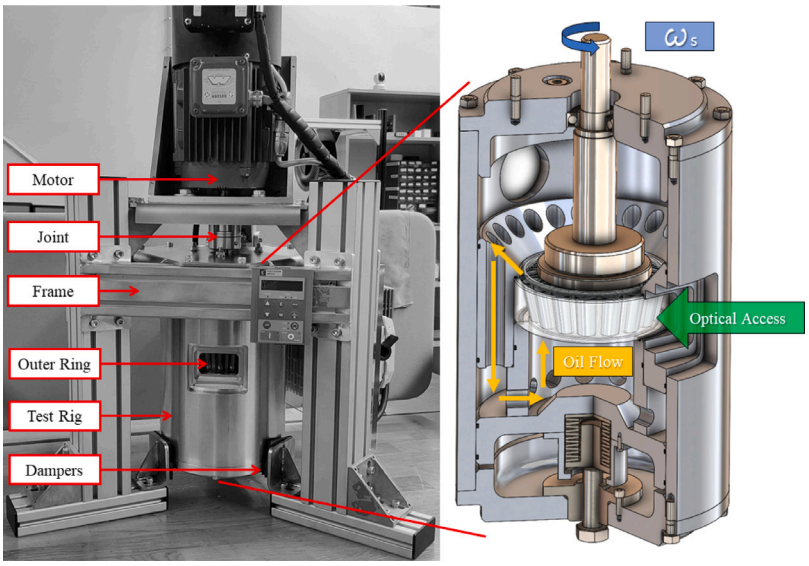

Fig. 1. Vertical Test Rig: assembly (left) and CAD model (right).

Table 2
Oil properties.

Symbol	Description	Value	Unit
ρ	Density	837	kg/m^3
$\mu_{40\ ^\circ C}$	Dynamic viscosity at 40 ° C	54.07	mPas
$\mu_{100\ ^\circ C}$	Dynamic viscosity at 100 ° C	9.96	mPas
A	Fitting parameter (coefficient) of the Andrade Equation	367.76	Pas
B	Fitting parameter (exponent) of the Andrade Equation	0.028	K

2.2. High speed imaging

In Fig. 2, the experimental setup used to capture high-speed images within the TRB during its operation at various speeds (i.e., 1000, 1500, 2000, and 2500 min^{-1}) and different oil levels (i.e., 0.1 Width and 1 Width) is shown. The rotational speed of 2500 min^{-1} is the maximum speed achievable by the test rig without causing excessive vibrations, thus ensuring accurate measurements. As observed, the optical access of the test rig was lighted by multiple light sources positioned at various angles to avoid reflections and ensure that the camera received sufficient light within the brief time the shutter remained open. The camera used was a Phantom® Miro M340, Ametek, Vision Research. The recording was conducted with a sample rate of 3200 frames per second (fps), corresponding to an interval time of 312.5 μs, with an effective exposure time of 9.11 μs. The resolution on the sapphire window was set to 1280 × 720 pixel^2, and the camera was positioned at a distance of 60 cm from the bearing window. A total of 500 frames were acquired and post-processed using the Phantom Camera Control application to identify any flow discrepancies between different sectors and the lubricant distribution at varying operational speeds. The video was recorded for a minimum of 100 rotations of the cage, corresponding to the observation of 1600 sectors (100 rotations and 16 sectors each rotations). After confirming that the variation of the flow between different sectors was minimal, a representative image was selected. This image is reported and discussed in detail in Section 5.1

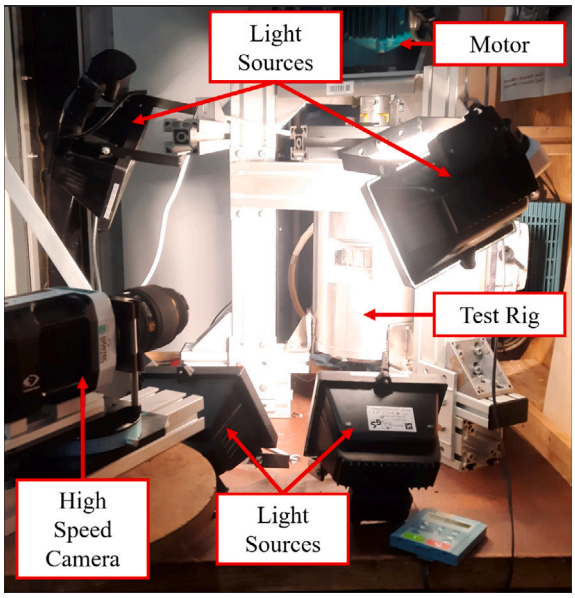

Fig. 2. Setup for High-Speed Camera Image Acquisition.

2.3. Particle image velocimetry

The oil was seeded with 10 μm fluorescent polystyrene particles. A fluorescent PIV approach was utilized to reduce noise in the presence of the metallic surfaces of the cage and rollers. Additionally, the steel cage in the target domain (Fig. 3) was polished to prevent particle deposition in its pores. In this research, velocity fields were examined using a stereoscopic approach (two cameras) with a LaVision's FlowMaster PIV system. The experimental setup is shown in Fig. 4. The cameras were arranged at a relative angle of 60° in the horizontal plane and inclined by 78° with respect to the vertical axis. These angles provided an optimal configuration for minimizing optical distortions and maximizing focus throughout the entire depth of the target domain (Fig. 3). The camera lenses were 105-mm, and the distance between these lenses and the target domain was approximately 250 mm. This setup captured

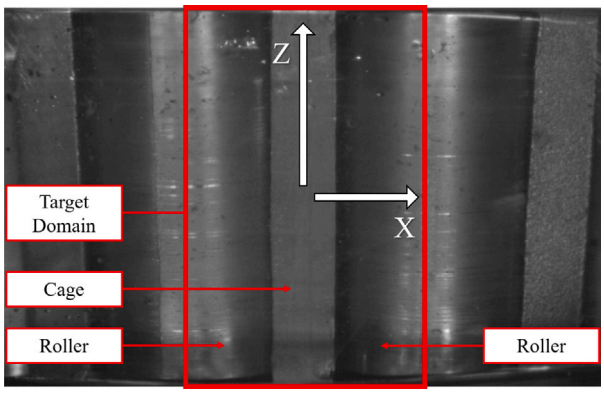

Fig. 3. View of the target domain and (X, Z) reference system.

the entire target domain, maximizing scanning resolution. The cameras used were 14-bit Imager Pro X 4M with a sensor size of 2048 × 2048 pixels^2 and a pixel dimension of 7.4 ×7.4 μm. To mitigate noise from the fluorescent light and accurately capture the fluorescent particles, the camera lenses were equipped with low-pass filters.

The laser employed was an EverGreen 200 dual-cavity with a maximum pulse energy of 200 mJ and a wavelength of 532 nm. Light-sheet forming optics were installed on the laser to generate a 15 mm vertical light sheet, illuminating the target domain. The laser was projected through a specialized tube with mirrors inside, enhancing the system's versatility and adjustability.

The maximum depth of the measured domain coincided with the distance between the outer race and the cage. This volume was centered between two rollers and included regions in proximity to the rollers (Fig. 3).

The positions of the cameras and the laser relative to the test rig were managed through a system of linear motion guides with perpendicular axes on which the cameras and laser were mounted. The calibration process was conducted using a specific device that allowed the insertion of a 3D calibration plate (LaVision 2-level plate with modified dimensions) inside a sapphire outer ring, filled with the tested oil. Additionally, the calibration device enabled positioning the plate at the same inclination as the cage (12° with respect to the bearing axis) and at a controllable distance from the outer race, centering the calibration plate in the middle of the target domain. This setup created a local reference system to decompose the measured velocity into different components. Specifically, the U_Z component was aligned with the vertical direction, positive according to the expected pumping effect (Fig. 3). The rotational speed leads the tangential average velocity of the cage U_{X0} to be positive along X.

To perform the calibration process, several steps are required. First, the calibration device is positioned within a dedicated structure 4. Subsequently, the cameras are aligned with respect to the calibration device using linear motion guides, adhering to the specified distances. After calibration, the cameras are repositioned in front of the target domain of the test rig, maintaining the same relative positioning.

A significant challenge in conducting PIV measurements in TRBs is synchronizing the camera with the cage rotation. The cameras must capture images within the target domain, which rotates with the cage. Synchronization was achieved using a magnetic trigger system. A magnet was attached to the cage, and a magnetic Hall effect sensor was placed on the outer part of the sapphire ring. These devices were circumferentially positioned to generate a trigger signal when the target domain was slightly upstream of the calibrated zone. By adjusting the time delay between the trigger signal and image recording, the PIV acquisition system was fine-tuned for various rotational speeds.

The magnetic trigger system allowed for the evaluation of the average rotational speed of the cage. The observed rotational speed closely

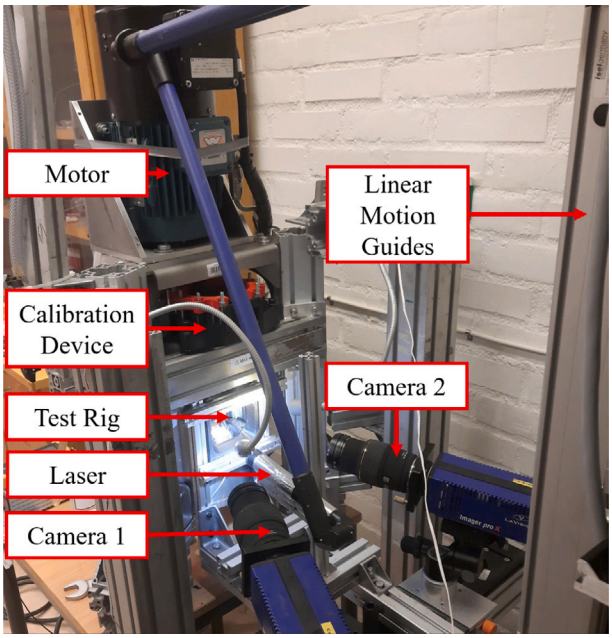

Fig. 4. Experimental set up for stereoscopic measurements.

matched the theoretical speed, calculated based on the shaft's rotational speed, with a discrepancy of less than 0.5%. This result confirms the accuracy of the bearing's kinematics, ensured by the applied axial load. During acquisition, each camera captured 100 dual image frames, i.e., two images with a time difference Δt (the inter-frame time), at each revolution of the cage for 100 rotations. Every time the magnet passed near the magnetic sensor, positioning the target domain within the calibrated volume, each camera captured two images at a specific inter-frame time. This process was repeated 100 times, corresponding to 100 cage rotations. This number of acquisitions has been tested in studies and results the best compromise to obtain stable and accurate results [29,30].

The Δt was adjusted according to the shaft's rotational speed (ω_S) to achieve the optimal signal-to-noise ratio for the final velocity fields. The inter-frame times used are shown in Table 3. The Δt for different rotational speeds was set to ensure the maximum particle shift between frames was less than one-third of the interrogation window size. The shaft speed varied from 1000 min^{-1} to 2500 min^{-1} (Table 3). Concurrently, the oil temperature (ϑ) was monitored, and the average cage velocity (U_{X0}), measured at half its height, is also reported. The estimated kinematic viscosity (ν) at the operating temperature is provided in the last column of Table 3 according to Eq. (1).

Since the case under study involves oil bath lubrication, the oil temperature varies depending on load-dependent and load-independent power losses, as well as the duration for which the bearing operates under steady-state conditions. It can be observed from the Table 3 that the equilibrium temperatures, achieved after approximately 1 min of operation under each condition, are higher in the case of a lower oil level ($W_{\%} = 10\%$).

3. Numerical approach: Mesh and boundary conditions

A CFD model has been implemented in OpenFOAM®i.e. an open-source CFD software package written in C++ that provides a highly customizable and flexible environment for simulating, among other physics, fluid dynamics. It operates efficiently on Linux-based systems and allows users to modify and extend solvers, utilities, and pre/post-processing tools to suit specific needs in research and engineering applications [37].

Table 3
Oil level (in percentage of the bearing width $W_{\%}$), Investigated rotational speeds (ω_S), related inter-frame times Δt, average cage velocities U_{X0}, monitored temperatures (ϑ), and evaluated kinematic viscosities (ν).

$W_{\%}$	ω_S	Δt	U_{X0}	ϑ	ν
%	min^{-1}	μs	m/s	°C	mm^2/s
10	1000	90	2.28	51	47.7
10	1500	60	3.42	57	40.3
10	2000	45	4.56	57	40.3
10	2500	36	5.70	59	38.1
100	1000	90	2.28	44	58.8
100	1500	60	3.42	46	54.9
100	2000	45	4.56	50	49.0
100	2500	36	5.70	51	47.7

The vertical orientation of the test rig allows the exploitation of the system's cyclic symmetry. Gravity acts axially, enabling the modeling of only a single sector of the TRB of this study. This sector involves cyclic symmetries passing through the centers of two neighboring rollers. The computational domain was discretized using the *blockMesh* utility, resulting in a mesh composed exclusively of hexahedral cells [30,38]. The mesh is created through 2 millions of cells having an average non-orthogonality of 9.83, and max skewness of 1.7. The computational domain encompasses a sector of the entire test rig, allowing for the full development of oil flows in both the upper and lower chambers of the test rig.

The volume modeled with *blockMesh* represents half of the sector, with the complete model created via a mirroring operation. The final model is illustrated in Fig. 5. In the figure, the "Shaft" patch (dark blue) represents all components rotating with the shaft, including the shaft and inner ring. The "outer ring" patch (white) includes all stationary components, such as the outer ring and other stationary parts of the test rig, including a channel that facilitates the return of oil from the upper chamber to the lower chamber. The cage is indicated in green and the rollers in red. Two cyclic Arbitrary Mesh Interfaces (AMIs) were applied to the lateral faces to model the cyclic symmetry of the test rig. Additional AMIs ("AMIs Inlet" and "AMIs Outlet") were applied at the upper and lower parts of the sector to simplify the modeling of the mesh outside the bearing. A small patch was created between the shaft and the frame to simulate a non-sealed bearing (NS Bearing). The relative pressure on this patch was set to zero. The gap between each roller, the inner ring, and the outer ring was created by scaling the roller relative to its center of gravity. Preliminary mesh and gap-sensitivity studies were conducted, suggesting a scale factor of 0.98, resulting in a gap of 0.05 mm. It is worth noting that the developed model does not account for deformations due to elasto-hydrodynamic contact. However, since the tests were conducted under minimal load to ensure the correct kinematics, what happens at the microscopic level (contact) does not affect the behavior of the oil at the macroscopic level (as observed experimentally). The initial conditions are shown in Fig. 6. The oil properties were set according to the temperatures recorded during the experimental session (Table 2).

In this study, a Rigid Mesh Motion (RMM) approach was implemented [1]. This approach involves a rigid motion of the mesh, rotating the bearing sector around the shaft axis. The mesh moved with the same rotational speed as the cage (ω_C). The velocities of other components were adjusted using specific Boundary Conditions (BCs) for the velocity field, such as an artificial added rotation of the roller around its own axis (ω_R) and an artificially superposed rotation for the rings (with the outer ring fixed and the inner ring rotating at ω_S). This method accurately reproduced the kinematics without any mesh deformation. Consequently, the physical velocities of the bearing components in the simulation differed from those used to move the boundary nodes and faces, naturally generating the apparent forces through the mesh movement. Additionally, this method allowed the consideration of field forces, such as gravity, which was set according to the test rig orientation.

Table 4
Boundary conditions 32312-A (U-velocity; p-relative pressure).

Patch	U	p
Roller 1	*conicalWallVelocity*	$\nabla p = 0$
Roller 2	*conicalWallVelocity*	$\nabla p = 0$
Outer Ring	*rotatingWallVelocity*	$\nabla p = 0$
Shaft	*rotatingWallVelocity*	$\nabla p = 0$
Cage	*movingWallVelocity*	$\nabla p = 0$
NS Bearing	*Inlet Outlet*	$p = 0$
CyclicAMIs	*cyclicAMI*	*cyclicAMI*
AMIs Inlet	*cyclicAMI*	*cyclicAMI*
AMIs Outlet	*cyclicAMI*	*cyclicAMI*

The kinematic of a TRB is represented in Fig. 7. In particular, in the figure, the angle of contact (ϕ), the mean diameter of the tapered roller (d_R), half the pitch diameter ($D_p/2$), the direction of the rotational speed of the Shaft (ω_S), of the Cage (ω_C), and of the Roller (ω_R) are defined.

The rotational speed of the cage (and thus the mesh), as well as the rotational speed of the roller, can be expressed as functions of the geometrical parameters (D_p, d_R, and ϕ) and the input velocity ω_S, as described in Eqs. (5) and (6) [39]. These equations implicitly assume that the outer ring is stationary. The negative sign of ω_R indicates that the roller rotates in the opposite direction relative to the inner ring.

$$\omega_C = \omega_S \frac{1}{2}\left[1 - \frac{d_R}{D_p}\cos(\phi)\right] \tag{5}$$

$$\omega_R = -\omega_S \frac{1}{2}\left\{\frac{D_p}{d_R}\left[1 - \left(\frac{d_R}{D_p}\cos(\phi)\right)^2\right]\right\} \tag{6}$$

The velocities were assigned to the patches using appropriate BCs. The *movingWallVelocity* BC, which translates the physical motion of patch points into a velocity field, allows the cage patch velocity to be directly extrapolated from the grid motion without requiring artificial corrections. The *rotatingWallVelocity* BC (with rotational axis and speed inputs defined via a dictionary) was used to impose the velocities of the rings. For the tapered rollers, which exhibit a combined motion of rotation around a fixed axis (shaft axis) and around a translating axis (roller axis), a new BC, named *conicalWallVelocity*, was implemented. This BC utilizes the motion of the faces (similar to the *movingWallVelocity BC*) to set the rotation of the roller around the bearing axis and adds an artificial velocity to replicate the pure rotation of the rolling element around its own axis. The applied BCs are summarized in Table 4.

4. Numerical approach: Solvers and processing

4.1. Standard solver for two incompressible, isothermal immiscible fluids using a Volume of Fluid Interface Tracking Method

CFD codes are based on the solution of three governing equations: mass, momentum, and energy conservation. In this study, the problem was modeled as isothermal. Therefore, the energy equation was not included in the calculation. Thus, the solution is limited to the mass (7) and momentum (8) equations [30], which, for incompressible fluid (expected Mach number less than 0.1) can be written as:

$$\nabla \cdot \mathbf{u} = 0 \tag{7}$$

$$\frac{\partial(\rho\mathbf{u})}{\partial t} + \nabla \cdot (\rho\mathbf{u}\mathbf{u}) = -\nabla p + \nabla \cdot (\bar{\bar{\tau}} + \bar{\bar{\tau}}_t) + \rho\mathbf{g} + \mathbf{f}_\sigma \tag{8}$$

Where $\mathbf{u}$ is the velocity vector, ρ is the density, p is the pressure, $\bar{\bar{\tau}}$ is the viscous stress tensor, $\bar{\bar{\tau}}_t$ is the Reynolds (turbulent) stress tensor, $\mathbf{g}$ is the gravitational acceleration vector, $\mathbf{f}_\sigma$ represents other body forces, i.e. surface tension.

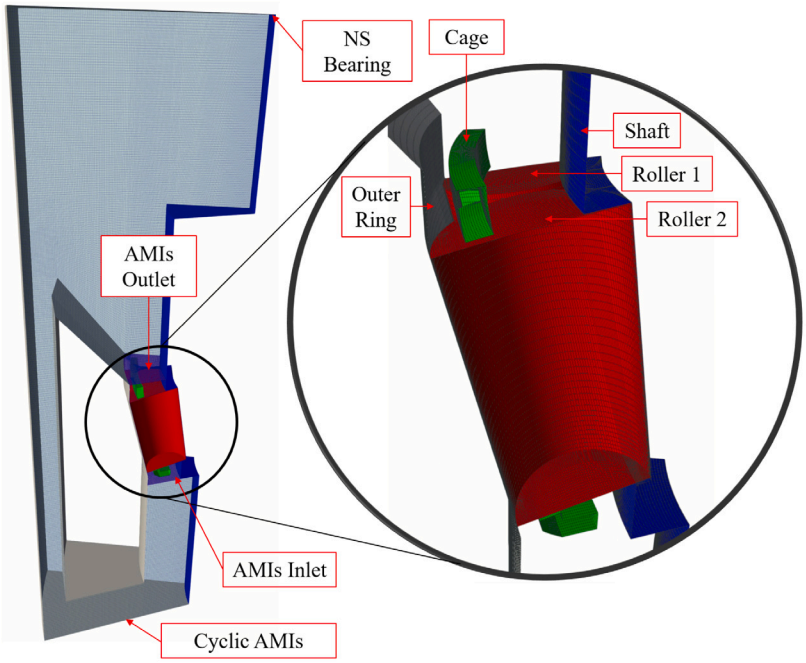

Fig. 5. Mesh and patches of the 32312-A model.

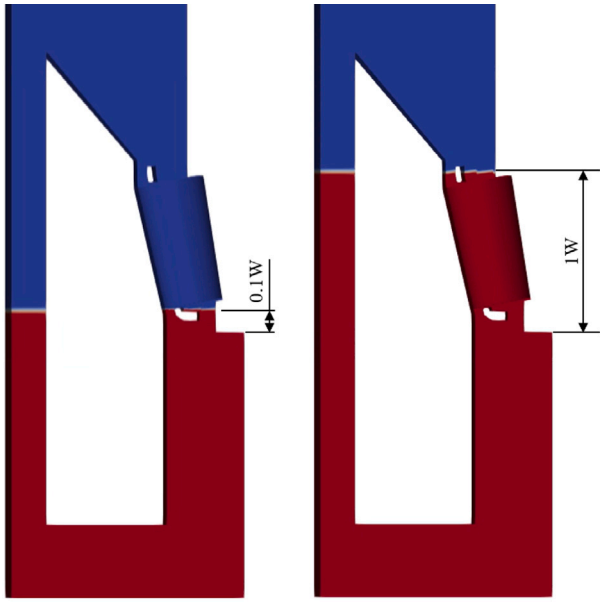

Fig. 6. Initial condition for oil distribution $W_{\%} = 10$ (left) and $W_{\%} = 100$ (right).

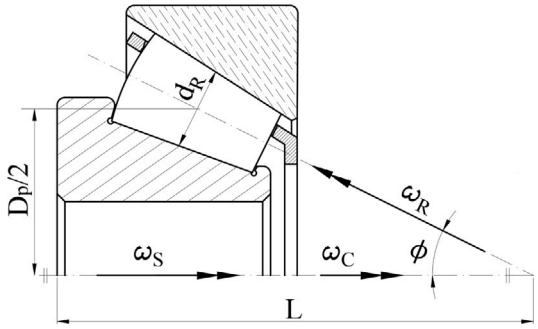

Fig. 7. Kinematic of a Tapered Roller Bearing.

Implementing the Re-Normalization Group (RNG) $k-\varepsilon$ model, according to [40], it is possible to express $\bar{\bar{\tau}}_t$ exploiting the eddy viscosity hypothesis (μ_t) as in Eqs. (9) and (10), [30].

$$\bar{\bar{\tau}}_t = \mu_t \left(\nabla \mathbf{u} + \nabla \mathbf{u}^T\right) - \frac{2}{3}\rho k \bar{\bar{I}} \tag{9}$$

$$\mu_t = C_\mu \rho \frac{k^2}{\varepsilon} \tag{10}$$

Where k is the turbulence kinetic energy, ε is the dissipation rate, $C_\mu = 0.085$ for RNG $k-\varepsilon$ turbulence model [40], $\bar{\bar{I}}$ is the identity matrix.

The conservation equations of the turbulent quantities according to the RNG $k-\varepsilon$ model are expressed in Eqs. (11) and (12), [30].

$$\frac{\partial(\rho k)}{\partial t} + \nabla \cdot (\rho k \mathbf{u}) = \nabla \cdot \left(\mu_{\text{eff}} \nabla k\right) + G_k + G_b - \rho\varepsilon + S_k \tag{11}$$

$$\frac{\partial(\rho \varepsilon)}{\partial t} + \nabla \cdot (\rho \varepsilon \mathbf{u}) = \nabla \cdot \left(\mu_{\text{eff}} \nabla \varepsilon\right) + C_{1\varepsilon} \frac{\varepsilon}{k}(G_k + C_{3\varepsilon} G_b) - C_{2\varepsilon} \rho \frac{\varepsilon^2}{k} - R_\varepsilon + S_\varepsilon \tag{12}$$

In these equations, G_k and G_b represent the turbulent kinetic energy generated from velocity gradients and buoyancy effects respectively. μ_{eff} is the sum of the dynamic viscosity and the turbulent viscosity. $C_{1\varepsilon}$, $C_{2\varepsilon}$, and $C_{3\varepsilon}$ are constants. S_k and S_ε are source terms. R_ε is a term derived from the renormalization group theory that characterizes the RNG model.

However, to solve multiphase problems, additional balance equations have to be considered. Indeed, in Eq. (8), ρ is defined by Eq. (13) through the volume fraction α. In the present study, the scalar α is equal to 1 if the cell is 100% oil and equal to 0 if the cell is 100% air. The same concept is extended to calculate the dynamic viscosity μ as in Eq. (14), [38].

$$\rho = \alpha \rho_{\text{oil}} + (1-\alpha)\rho_{\text{air}} \tag{13}$$

$$\mu = \alpha \mu_{\text{oil}} + (1-\alpha)\mu_{\text{air}} \tag{14}$$

Moreover, Eq. (15), related to the volumetric fraction, has to be solved [38].

$$\frac{\partial \alpha}{\partial t} + \nabla \cdot (\alpha \mathbf{u}) = 0 \tag{15}$$

4.2. Specific solver for considering aeration using a volume of fluid

In this work, aeration is modeled according to the Hirt model [41,42]. In this model, air is entrained into the liquid phase when the turbulent energy per unit volume exceeds the stabilizing forces of gravity and surface tension per unit volume. Therefore, an additional source term (S_g) is added to the equation of the volumetric fraction to account aeration as in Eq. (16):

$$\frac{\partial \alpha}{\partial t} + \nabla \cdot (\alpha \mathbf{u}) + \nabla \cdot (\mathbf{u}_c \alpha (1-\alpha)) = S_g \tag{16}$$

Here, $\mathbf{u}_c$ represents the characteristic velocity associated with the coalescence or other specific phenomena within the multiphase flow context [43]. The source term, which is included explicitly in the conservation equation for the volumetric fraction field, is defined as in Eq. (17), [30].

$$S_g = C_{\text{air}} A_S \sqrt{\frac{2(P_t - P_d)}{\rho}} \tag{17}$$

where S_g is the volume of air per unit time $\left(\frac{\delta V}{\delta t}\right)$, C_{air} is a calibration parameter, A_S is the free surface area of each cell, and ρ is the fluid density. The term P_t is given by Eq. (18), [30].

$$P_t = \rho k \tag{18}$$

where P_t represents the turbulent forces. The stabilizing forces, P_d, are defined as in Eq. (19), [30].

$$P_d = \rho g_n L_T + \frac{\sigma}{L_T} \tag{19}$$

where g_n is the component of gravity normal to the free surface, σ is the surface tension, and L_T is the turbulence characteristic length scale, formulated as in Eq. (20), [30].

$$L_T = C_\mu \left(\frac{k^{3/2}}{\varepsilon}\right) \tag{20}$$

with $C_\mu = 0.085$ for the RNG $k-\varepsilon$ turbulence model [40].

The Hirt model accounts for the increase in fluid volume due to the addition of air and the buoyancy effects associated with entrained air. It balances the stabilizing forces of gravity and surface tension against the destabilizing effects of surface turbulence. Given that turbulence is the primary cause of entrainment, a turbulence-transport model must be used in conjunction with the air-entrainment model. Air entrapment occurs as turbulent eddies lift small liquid elements above the free surface, potentially trapping air and carrying it back into the liquid. For air trapping to occur, the turbulent kinetic energy per unit volume, P_t, must be greater than P_d. If P_t is less than P_d, then δV is zero, and no air is added. The value of C_{air} ranges between 0 and 1, with a recommended initial value of $C_{\text{air}} = 0.5$, based on the assumption that air will be entrained over approximately half of the surface area. This value has been validated in all tests by Hirt [41].

4.3. Settings and processing

The entire Design of Experiment (DoE), comprising 4 rotational speeds and two oil levels, was simulated using both a Standard solver, as described in Section 4.1, and a solver accounting for aeration, detailed in Section 4.2, resulting in a total of 16 simulations.

Simulations were performed with an adjustable time step limiting the Courant number $CLF < 1$ to ensure numerical stability and convergence and, at the same time, maximizing the simulation speed. The simulations were stopped after five complete revolutions of the cage (equivalent to five revolutions of the mesh sector). By parallelizing the simulations on a High Performance Computing (HPC) Cluster equipped with AMD EPYC 7232P 24-Core Processors operating at 3.10 GHz (297.6 GFLOPs), each simulation was completed in approximately 80 h for the solver including aeration and 70 h for the standard solver. The fields from each simulation were saved every 1/16 of a bearing revolution (corresponding to one save for each sector rotation, given that the bearing has 16 rollers). Eventually, velocity, pressure, volumetric fraction, and other fields were averaged over the 80 equidistant time steps obtained during the physical time of the simulation to be comparable with the PIV acquisitions (that are averaged values).

5. Results and discussion

5.1. Oil distribution

In this section, both experimental and numerical results are presented for various operating conditions. Specifically, Fig. 8 shows the results for an initial oil level of 10% of the bearing width, and Fig. 9 presents the results for an initial oil level of 100% of the bearing width. Each column in the figures represents a different rotational speed, ranging from 1000 min^{-1} on the left to 2500 min^{-1} on the right. In the figures, the cage motion is from left to right. Each row corresponds to a different approach and/or processing method:

- The first row of Figs. 8 and 9 (labeled Camera) presents the experimental results acquired with a HSC, limited to the target domain. Particularly in Fig. 8, the cage is visible in the central part of the image, especially clear in the lower part where it is not covered by the lubricant. There is a noticeable higher concentration of oil on the left side of the target domain compared to the right side, indicating the rollers are moving from left to right; the left roller, more visible due to less oil coverage, is the "leading roller". In other words, it can be observed that the lower right area is predominantly filled with air, allowing a clear view of both the cage and part of the right roller.
- The second row of Figs. 8 and 9 (labeled Aeration - avg) shows results obtained with the CFD solver that includes aeration. Five revolutions of the cage were simulated, with data saved at regular intervals (every 22.5 degrees, corresponding to the modeled sector angle), resulting in 80 savings. The volume fraction (α), velocity, pressure, and other fields were averaged across these savings. The second row displays the averaged volume fraction α, with cells having $\alpha > 0.5$ (indicating at least half of the cell volume filled with lubricant) shown in varying transparency levels. Higher transparency indicates areas with a lower average oil quantity.
- The third row of Figs. 8 and 9 (labeled Aeration - inst) also uses the aeration-inclusive solver but shows the instantaneous result after five cage revolutions, representing the latest time step. Similar transparency levels and the $\alpha > 0.5$ threshold are maintained. This result can be more directly compared with experimental measurements but is subject to variability due to the simulation's dynamic nature.
- The fourth row of Figs. 8 and 9 (labeled Standard - avg) presents results from a standard bi-phase solver without aeration and with Volume of Fluid (VoF) interface tracking. These results were processed similarly to those in the second row: five cage revolutions, 80 equidistant savings, and averaged results. Cells with $\alpha > 0.5$ are shown with varying transparency based on the average α level.
- The fifth row of Figs. 8 and 9 (labeled Standard - inst) displays the instantaneous results using the standard bi-phase solver at the last simulated time step, similar to the third row but with a Standard Solver. In this case, the α-gradient between 0 and 1 is a numerical diffusivity of the interface.

Comparing the experimental observations (first row of Figs. 8 and 9), a higher oil presence is evident in Fig. 9. However, with increasing rotational speed (e.g., 2500 min^{-1} for $W_{\%} = 100\%$), the oil distribution profile resembles that of lower oil levels, showing more oil at the larger diameter (upper part) and less at the smaller diameter (lower part)

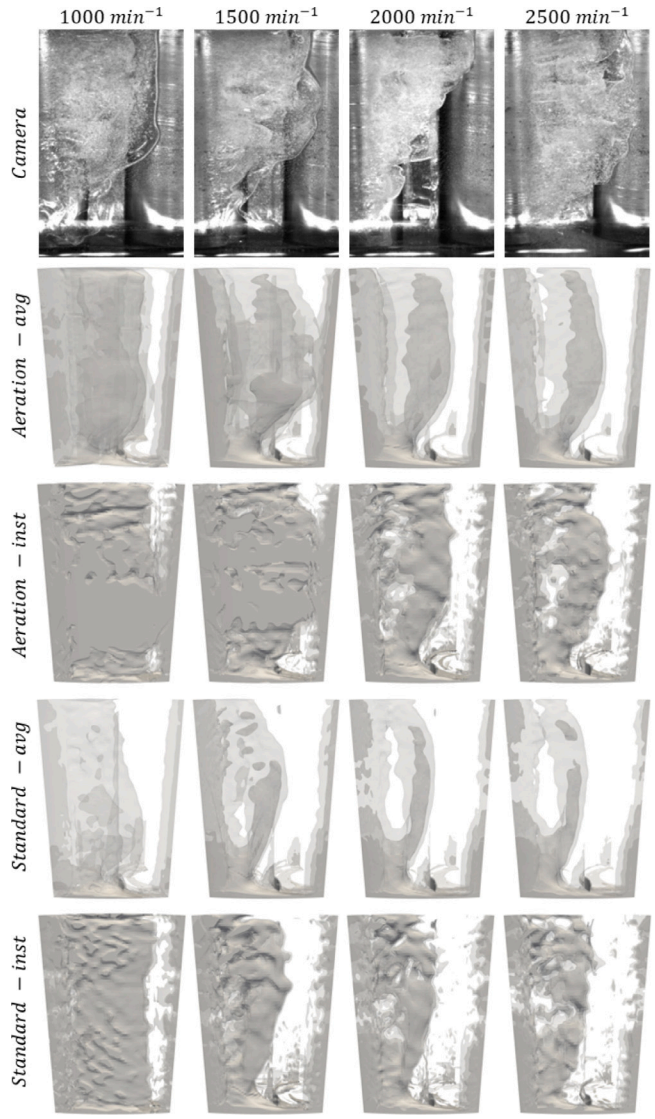

Fig. 8. Oil distribution for initial oil level of $W_{\%} = 10\%$ at different rotational speeds (from left to right: 1000, 1500, 2000, 2500 min^{-1}) and various processing methods: acquisition with HSC (first row: Camera), averaged result with aeration solver (second row: Aeration - avg), instantaneous result after 5 revolutions of the cage with aeration solver (third row: Aeration - inst), averaged result with standard bi-phase solver (fourth row: Standard - avg), instantaneous result after 5 revolutions of the cage with standard bi-phase solver (last row: Standard - inst). In the figures, the cage motion is from left to right.

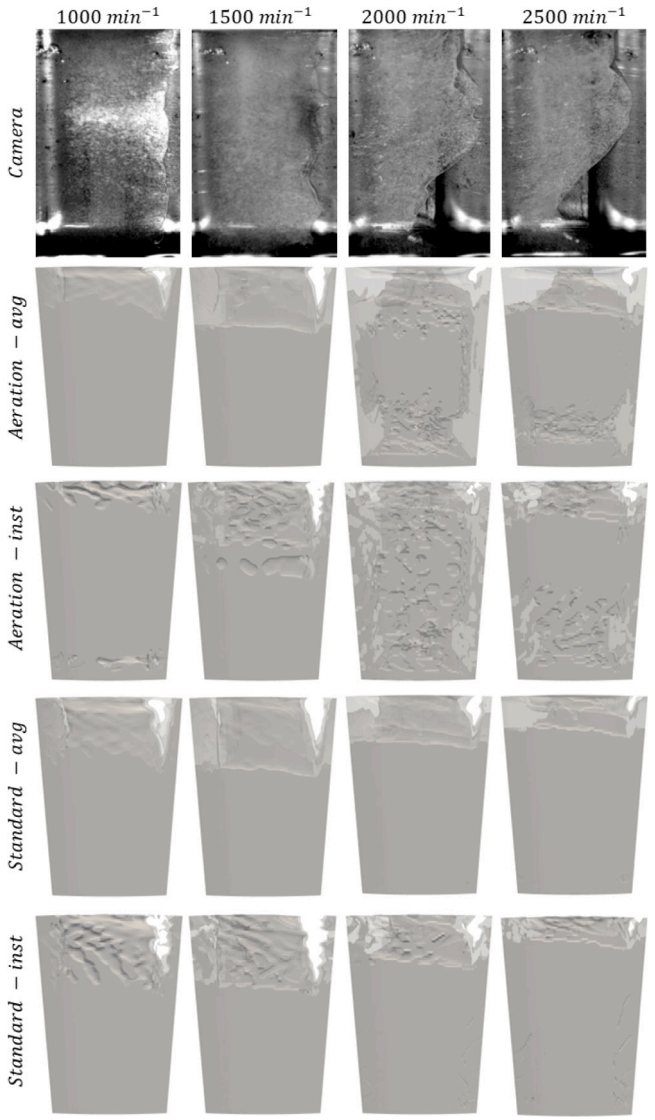

Fig. 9. Oil distribution for initial oil level of $W_{\%} = 100\%$ at different rotational speeds (from left to right: 1000, 1500, 2000, 2500 min^{-1}) and various processing methods: acquisition with HSC (first row: Camera), averaged result with aeration solver (second row: Aeration - avg), instantaneous result after 5 revolutions of the cage with aeration solver (third row: Aeration - inst), averaged result with standard bi-phase solver (fourth row: Standard - avg), instantaneous result after 5 revolutions of the cage with standard bi-phase solver (last row: Standard - inst). In the figures, the cage motion is from left to right.

of the bearing. These profiles differ significantly from the hypotheses formulated in the 1970s [32] for solving its analytical model, i.e. an uniform laminar flow that has a parabolic velocity profile along its thickness. The images also reveal oil aeration, with micro-bubbles trapped within the oil and specific fluxes profiles.

Numerical results in Fig. 8 show that both the Aeration and Standard simulations predict a higher oil concentration in the upper part and around the rear roller (left side of the cage). However, the Standard simulation tends to underestimate the oil quantity in the target domain, possibly due to overestimating the aerated fluid's macroscopic density, which is more susceptible to inertia forces. Additionally, Standard simulations do not effectively capture the oil distribution at lower speeds. While Aeration simulations capture the macroscopic oil distribution, they do not precisely match experimental observations, with the 1500 min^{-1} case being the closest.

In Fig. 9, the results are harder to interpret due to the abundant oil presence. The Aeration model indicates a lower fluid density (volume fraction) in the lower part for speeds of 2000 min^{-1} and 2500 min^{-1}, an effect not seen in the Standard solutions but observed experimentally. Both solvers tend to predict a reduction in volume fraction in the upper part, which was not observed experimentally with the resolution achieved in this study. However, it is worth noting that for the solver that accounts for aeration, having a diffuse α value indicates the presence of a certain percentage of air within the oil. In contrast, for the standard solver, this is merely a computational error, i.e. a numerical diffusion of the interfaces between oil and air.

Figs. 10 and 11 present additional information on the oil distribution beyond the target domain obtained from CFD simulations. Specifically, Fig. 10 displays the source term S_g mentioned in Eq. (17) for the aeration solver. For brevity, the results are shown only for a rotational speed of 2500 min^{-1} after 5 cage rotations, representing

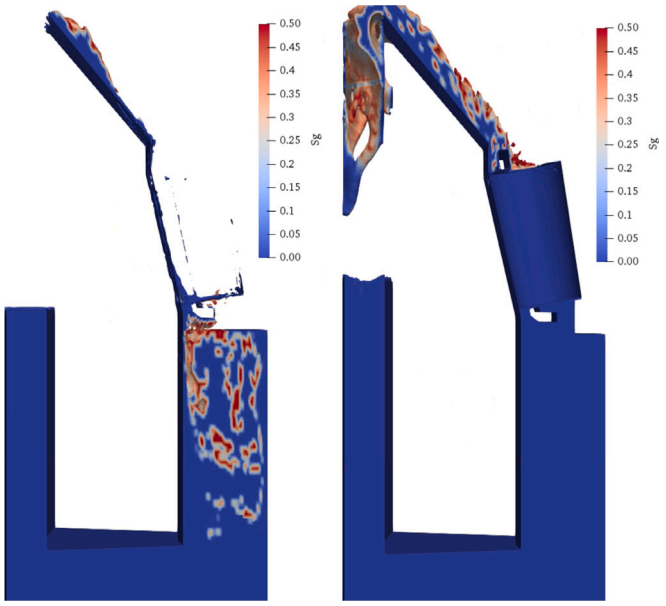

Fig. 10. Source term S_g described in Eq. (17) for the solver with aeration, filtered for a volume fraction $\alpha > 0.5$. Results are shown for a speed of 2500 min^{-1} after 5 revolutions of the cage, with $W_{\%} = 10\%$ on the left and $W_{\%} = 100\%$ on the right.

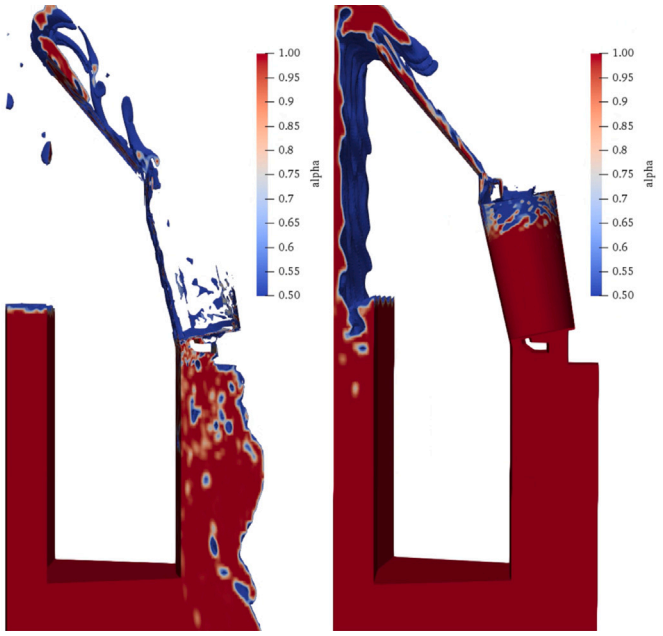

Fig. 11. Oil distribution achieved with the standard bi-phase solver, filtered for a volume fraction $\alpha > 0.5$. Results are shown for a speed of 2500 min^{-1} after 5 revolutions of the cage, with $W_{\%} = 10\%$ on the left and $W_{\%} = 100\%$ on the right.

various operating conditions. The left image shows results for an initial oil level of $W_{\%} = 10\%$, while the right image shows results for $W_{\%} = 100\%$. The field is filtered for $\alpha > 0.5$ to highlight cells where at least 50% of the volume is occupied by lubricant. The color gradient, from blue to red, indicates the value of the source term S_g, i.e., the volume of air entrapped per unit time. Notably, for a low initial oil level, air inclusion occurs both in the lower chamber of the test rig (where oil is "sucked" by the bearing) and in the upper part (where oil is pumped by the bearing). Conversely, with a higher initial oil level (right image), air inclusion is primarily observed in the upper chamber of the test rig. These images suggest that, over a sufficiently long simulation time, oil aeration would likely increase further as the pumped oil re-enters the bearing from the lower part. However, such extended simulations were not conducted in this study due to excessive computational time requirements.

Fig. 11 shows the volume fraction α that results from simulations using the Standard solver. Also in this case, results are shown only for a rotational speed of 2500 min^{-1} after 5 cage rotations, representing various operating conditions, and filtered for $\alpha > 0.5$ to distinguish oil-prevalent zones. Here, the color scale is inverted compared to the previous case; blue indicates a high percentage of air in the cell (below 50% of the cell volume), while red indicates a high percentage of oil (above 50% of the cell volume). A minimal numerical diffusivity is present. The left image shows results for an initial oil level of $W_{\%} = 10\%$, while the right image shows results for $W_{\%} = 100\%$.

In the left image, with a lower initial oil level, a sharp separation surface between air and oil is observed in the lower chamber, near the shaft. Blue areas indicate regions where the volume fraction is not unitary, but without aeration, the oil–air interface remains almost sharp. For the higher initial oil level case (right image), air primarily enters the bearing's upper part. The pumped flow towards the test rig's upper chamber remains well-separated from the air and moves faster compared to the aerated case.

5.2. Velocity field

This section presents the velocity field results measured via PIV and estimated through CFD simulations. Specifically, Fig. 12 displays results for an initial condition of $W_{\%} = 10\%$, while Fig. 13 shows results for $W_{\%} = 100\%$. The velocity field is depicted within the target domain, considering the area between two rollers and the space between the cage and the outer race.

- The first row of Figs. 12 and 13 (labeled PIV - U_Z/U_{X0}) shows the dimensionless axial velocity field (U_Z/U_{X0}) measured experimentally using PIV. The ensemble average was obtained using LaVision PIV processing software Davis 10. For each dual frame, velocity vectors were processed with the multi-pass PIV algorithm, resulting in a final interrogation window size of 64 × 64 pixels with 75% overlap. The displayed velocity is averaged over 100 cage rotations. The axial velocity is highlighted as it demonstrates the pumping effect of TRBs.
- The second row of Figs. 12 and 13 (labeled Aeration - U_Z/U_{X0}) presents the same results but obtained through CFD using the aeration solver. As in previous cases, the velocity field results were averaged over 80 savings collected during 5 cage rotations. The data were taken on a plane parallel to the cage's vertical strip, positioned between the cage and the outer race.
- The third row of Figs. 12 and 13 (labeled Standard - U_Z/U_{X0}) shows results obtained using a standard bi-phase CFD solver. As well as the second row, the velocity field results were averaged over 80 data points from 5 cage rotations and collected on the same plane.

Comparing the experimental results in Figs. 12 and 13, the distinctive shape of the experimentally obtained velocity profile is evident. In both $W_{\%} = 10\%$ and $W_{\%} = 100\%$ conditions, there is an increase in the area of maximum axial velocity with rising rotational speed. However, the intensities observed with $W_{\%} = 10\%$ are generally higher than those recorded for $W_{\%} = 100\%$, likely due to the higher static pressure from the greater oil mass. Additionally, the region of maximum axial velocity is recorded at the lower diameter, initially near the right roller (leading roller), probably due to the suction effect of the moving roller, then quickly shifts towards the left roller before diffusing upwards, approaching the right roller again while decreasing in intensity.

Comparing the experimental results with CFD simulations, it is notable that the aeration solver results exhibit characteristics more similar

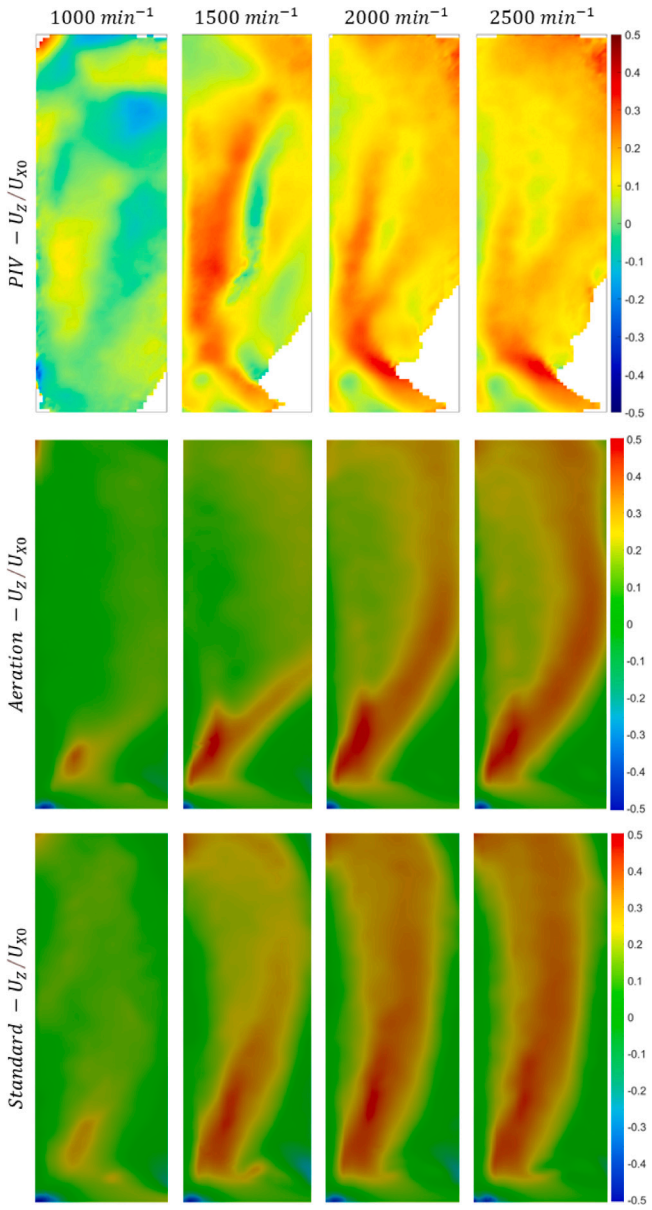

Fig. 12. $W_{\%} = 10\%$ - Axial velocity field (U_Z) normalized with respect to the average cage velocity (U_{X0}) for different rotation speeds (from left to right: 1000, 1500, 2000, 2500 min^{-1}) and various processing methods: PIV measures (first row: PIV - U_Z/U_{X0}), CFD result with aeration solver (second row: Aeration - U_Z/U_{X0}), CFD result with standard bi-phase solver (third row: Standard - U_Z/U_{X0}).

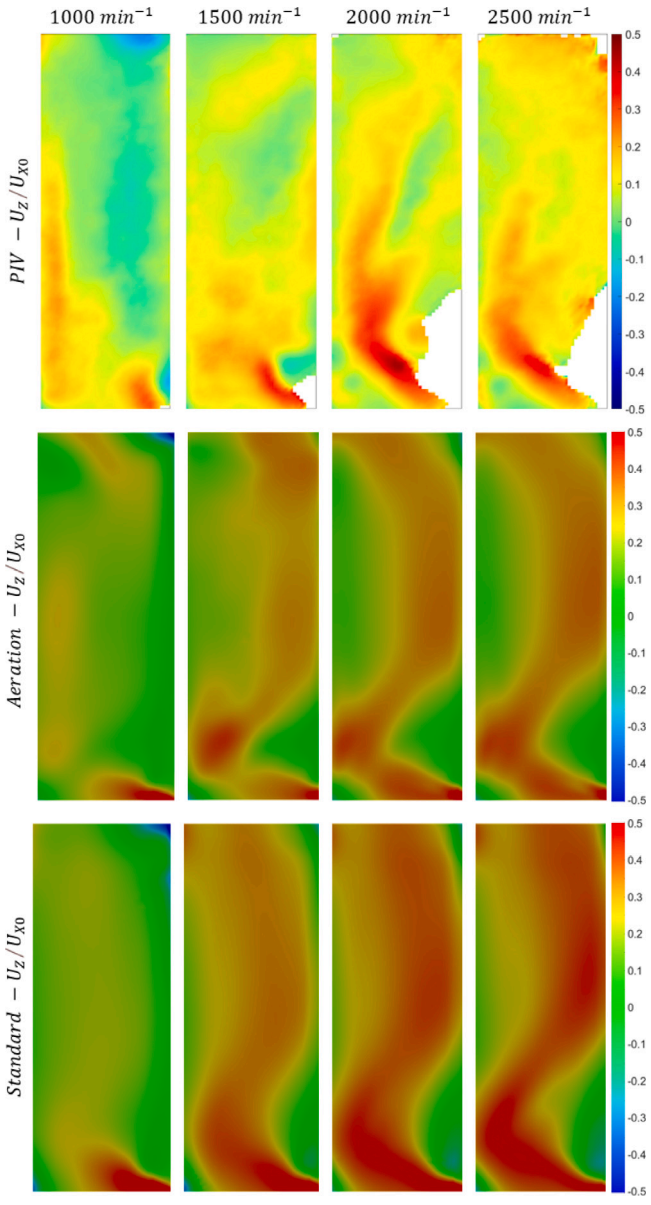

Fig. 13. $W_{\%} = 100\%$ - Axial velocity field (U_Z) normalized with respect to the average cage velocity (U_{X0}) for different rotation speeds (from left to right: 1000, 1500, 2000, 2500 min^{-1}) and various processing methods: PIV measures (first row: PIV - U_Z/U_{X0}), CFD result with aeration solver (second row: Aeration - U_Z/U_{X0}), CFD result with standard bi-phase solver (third row: Standard - U_Z/U_{X0}).

to the experimental outcomes than those obtained with the standard solver. Specifically, the standard solver, especially in Fig. 12, displays a less curved velocity profile, with the red area rising almost equidistant from both rollers, whereas the experimental and aeration solver results show more points of curvature. Furthermore, in Fig. 13, the standard solver tends to overestimate both the value and extent of the maximum axial velocity, whereas the aeration solver provides more accurate trends. It is interesting to note that both solvers capture the curvature variation in the lower part, as observed experimentally. Although the standard solver shows discrepancies in the absolute velocity value, it seems to capture the flow patterns well as the oil presence increases. In the experimental measurements, it can be observed that there are no velocity field acquisitions in the lower right section. This result is consistent with the HSI observations, as that area is predominantly filled with air, and since the fluorescent seeding is present only in the lubricant, the velocity field could not be mapped there. On the other hand, in the reported CFD data, no filter for volume fraction was applied, and the velocity field of the oil was not differentiated from that of the air.

5.3. General discussions

In general, it can be stated that through the acquisition of images using HSC, the oil distribution within the target domain was qualitatively observed. Video inspection revealed that, with equal rotation speeds and initial oil levels, different sectors of the same bearing showed a similar oil distribution, with minor variations due to the system's intrinsic dynamic effects. Additionally, the observation of images obtained through HSC indicated that aeration is a phenomenon present in oil-lubricated bearings at various speeds and oil levels. However, it was not possible to quantify whether the number and/or size of air

bubbles trapped in the oil varied under different operating conditions. Qualitatively, it was noted that the number of bubbles seems to increase with higher speeds. In future studies, ultrasonic methods could be applied to quantify the level of aeration, as proposed in [26]. These techniques have the potential to provide a more accurate and non-invasive way to measure aeration within lubricating systems, offering valuable insights for improving fluid dynamics analysis.

Quantitative velocity field measurements were achieved using PIV. However, due to the two-dimensional nature of the computational domain and the inability to measure the lubricant's thickness, it was not possible to accurately quantify the axial flow rate resulting from the pumping effect. Nonetheless, the axial velocity field displayed a characteristic shape at different speeds. It appears that the flow is drawn from below by the depression field created by the leading roller and, once it enters the target domain, it is pushed by the trailing roller and accelerated towards the bearing's larger diameter.

These two types of experimental observations enabled the evaluation of results obtained through the two numerical strategies discussed in this paper, i.e., a CFD study involving an immiscible bi-phase solver with VoF interface tracking and a solver accounting for aeration. The results were compared in terms of oil distribution and velocity fields. It was found that, despite some limitations, the aeration-accounting solver could more accurately capture certain physical effects related to oil distribution and the resulting velocity field under various operating conditions. However, the numerical results are based on simulations of 5 cage rotations, which, according to literature, should be sufficient to stabilize the results [30,31,44]. Nonetheless, it was observed that the aerated oil in the upper part of the bearing did not complete a full recirculation, suggesting that simulations halted after 5 rotations might underestimate the overall aeration level of the oil entering the target domain, especially in cases of higher oil levels (since, for low oil level, aeration appears also in the lower chamber of the test rig).

Eventually, it is worth mentioning that the developed model has been validated for a maximum speed of 2500 min^{-1}. However, since an increase in aeration levels was observed with rising speed, it is plausible to assume that the model can estimate the oil behavior at higher rotational speeds as well. Nevertheless, this assumption will need to be validated in future studies, as new phenomena, such as cavitation, may need to be considered at higher speeds.

6. Conclusions

This study explored the oil distribution within a TRB under various operating conditions using both experimental and numerical approaches. HSC imaging and Particle Image Velocimetry were employed to capture and quantify the lubricant behavior within the bearings. Additionally, Computational Fluid Dynamics (CFD) simulations using OpenFOAM® were conducted to complement and validate the experimental observations.

The investigation revealed distinct oil distribution patterns at different rotational speeds and initial oil levels. For a lower oil level ($W_{\%} = 10\%$), both experimental and CFD results indicated higher oil concentrations in the upper part of the bearing, with significant aeration occurring at higher speeds. At a higher oil level ($W_{\%} = 100\%$), the oil distribution was more uniform, though aeration effects remained notable, particularly at 2500 min^{-1}. The aeration solver provided more accurate representations of the experimental results compared to the standard bi-phase solver, capturing the regions of high axial velocity and the overall oil movement within the bearing more effectively.

The analysis of the velocity field, as measured by PIV and estimated through CFD simulations, highlighted the inherent pumping effect of TRBs. The velocity field results from the aeration solver closely match the experimental measurements, whereas the standard solver tends to overestimate axial velocities and fail in capturing the intricate flow patterns observed experimentally. This demonstrates the importance of considering aeration effects in simulating lubricant behavior in TRBs.

The CFD model incorporating the aeration solver successfully replicated the experimental findings, validating its reliability for future studies on lubricant dynamics in rolling bearings. This study underscores the critical role of aeration in influencing oil distribution and velocity fields within TRBs, suggesting that future research should extend the simulation time to observe long-term aeration effects and further refine the CFD model to enhance its predictive capabilities. Additionally, exploring different lubrication conditions and bearing geometries could provide broader insights into optimizing TRB performance under various operational scenarios.

In comparison with the results obtained in previous studies, conducted exclusively under fully-flooded lubrication conditions (without aeration in [31] and with aeration in [30]) the present study has revealed interesting flow patterns under oil-bath lubrication conditions. It allowed the observation of areas where oil tends to accumulate and where air is predominantly present. This finding, observed for the first time in this work, differs significantly from the hypothesis reported in [32].

Eventually, the development of this CFD model and the experimental procedure opens the door to a range of potential future studies aimed at observing and/or predicting oil behavior within rolling element bearings and assessing the impact of design improvements. New cage geometries could be explored to ensure proper lubricant flow in the contact areas, and new axial-flow deflectors could be designed and studied. Additionally, the effectiveness of different types of additives could be experimentally tested using the proposed experimental procedure.

Nomenclature

HSC	High-Speed Camera
HSI	High-Speed Imaging
LIF	Laser-Induced Fluorescence
fps	frame per second
BC	Boundary Condition
CFD	Computational Fluid Dynamics
TRB	Tapered Roller Bearing
PIV	Particle Image Velocimetry
BIV	Bubble Image Velocimetry
DoE	Design Of Experiment
VoF	Volume of Fluid
AMI	Arbitrary Mesh Interface
RMM	Rigid Mesh Motion
HPC	High Performance Computing
RNG	Re-Normalization Group
EIS	Electrical Impedance Spectroscopy
A	Fitting parameter (coefficient) of the Andrade Equation
B	Fitting parameter (exponent) of the Andrade Equation
CLF	Courant Number
ρ	Density
ω_S	Rotational speed of the shaft
ω_C	Rotational speed of the cage
ω_R	Rotational speed of the roller
d_R	Mean diameter of the tapered roller
D_p	Pitch diameter of the tapered roller bearing
L	Distance between the main bearing shoulder and the intersection of the shaft and roller rotation axes
ϕ	Angle between the shaft and roller rotation axes
Δ_t	Inter-Frame Time
$W_{\%}$	Percentage of the bearing width initially covered by the oil
ϑ	Temperature
ν	Kinematic viscosity
μ	Dynamic viscosity

μ_t	Dynamic eddy (turbulent) viscosity
μ_{eff}	sum of the dynamic eddy (turbulent) viscosity and the dynamic viscosity
$C_{1\varepsilon}, C_{2\varepsilon}, C_{3\varepsilon},$	Constants
S_k, S_ε	Source terms
R_ε	RNG term
α	Volume fraction
$\mathbf{u}_c$	Characteristic velocity
S_g	Source term: volume of air per unit of time
C_{air}	Calibration parameter
A_S	Free surface area of each cell
P_t	Turbulent forces
P_d	Stabilizing forces
σ	Surface tension
L_T	Turbulence characteristic length scale
δV	Variation of volume of air trapped in the oil
$\mathbf{u}$	Velocity vector
$\bar{\bar{\tau}}$	Viscous stress tensor
$\bar{\bar{\tau}}_t$	Reynolds (turbulent) stress tensor
$\mathbf{g}$	Gravitational acceleration vector
$\mathbf{f}_\sigma$	other body forces i.e. surface tension
k	Turbulent kinetic energy
ϵ	Dissipation rate
$\bar{\bar{I}}$	Identity matrix
G_k	Turbulent kinetic energy generated from velocity gradients
G_b	Turbulent kinetic energy generated from buoyancy effects

Funding

The present study is supported by the project "Cfd simUlations of BEaring" ("CUBE"), funded by Schaeffler Technologies AG & Co. KG (PI Franco Concli).

CRediT authorship contribution statement

Lorenzo Maccioni: Writing – review & editing, Writing – original draft, Visualization, Validation, Software, Methodology, Investigation, Formal analysis, Data curation, Conceptualization. **Valery G. Chernoray:** Software, Resources, Methodology, Investigation, Formal analysis, Data curation. **Franco Concli:** Writing – review & editing, Writing – original draft, Supervision, Software, Resources, Project administration, Methodology, Investigation, Funding acquisition, Conceptualization.

Declaration of competing interest

The authors declare that they have no known competing financial interests or personal relationships that could have appeared to influence the work reported in this paper.

Data availability

The authors do not have permission to share data.

References

[1] Maccioni L, Concli F. Computational fluid dynamics applied to lubricated mechanical components: Review of the approaches to simulate gears, bearings, and pumps. Appl Sci (Switzerland) 2020;10(24):1–29. http://dx.doi.org/10.3390/app10248810.

[2] Sadeghi F, Arya U, Aamer S, Meinel A. A review of computational fluid dynamics approaches used to investigate lubrication of rolling element bearings. J Tribol 2024;1–39. http://dx.doi.org/10.1115/1.4065663.

[3] Wang L, Powrie H. Advanced techniques for bearing condition monitoring. 2024, p. 153–81. http://dx.doi.org/10.1016/B978-0-443-14074-7.00009-1,

[4] Pastukhov A, Timashov E, Stanojević D. Temperature conditions and diagnostics of bearings. Appl Eng Lett 2023;8(2):45–51. http://dx.doi.org/10.18485/aeletters.2023.8.2.1.

[5] Alvarado-Hernandez AI, Zamudio-Ramirez I, Jaen-Cuellar AY, Osornio-Rios RA, Donderis-Quiles V, Antonino-Daviu JA. Infrared thermography smart sensor for the condition monitoring of gearbox and bearings faults in induction motors. Sensors 2022;22(16). http://dx.doi.org/10.3390/s22166075.

[6] Jakubek B, Grochalski K, Rukat W, Sokol H. Thermovision measurements of rolling bearings. Meas J Int Meas Confed 2022;189. http://dx.doi.org/10.1016/j.measurement.2021.110512.

[7] Wu W, Hu C, Hu J, Yuan S. Jet cooling for rolling bearings: Flow visualization and temperature distribution. Appl Therm Eng 2016;105:217–24. http://dx.doi.org/10.1016/j.applthermaleng.2016.05.147.

[8] Wen Y, Oshima S. Oil flow simulation based on CFD for reducing agitation torque of ball bearings. SAE Int J Passeng Cars Mech Syst 2014;7(4):1385–91. http://dx.doi.org/10.4271/2014-01-2850.

[9] Santhosh R, Hee JL, Simmons K, Johnson G, Hann D, Walsh M. Experimental investigation of oil shedding from an aero-engine ball bearing at moderate speeds. In: Turbo expo: power for land, sea, and air. 50923, American Society of Mechanical Engineers; 2017, V07AT34A018. http://dx.doi.org/10.1115/GT2017-63815.

[10] Russell T, Sadeghi F, Peterson W, Aamer S, Arya U. A novel test rig for the investigation of ball bearing cage friction. Tribol Trans 2021;64(5):943–55. http://dx.doi.org/10.1080/10402004.2021.1953657.

[11] Aamer S, Sadeghi F, Russell T, Peterson W, Meinel A, Grillenberger H. Lubrication, flow visualization, and multiphase CFD modeling of ball bearing cage. Tribol Trans 2022;65(6):1088–98. http://dx.doi.org/10.1080/10402004.2022.2123420.

[12] Chen H, Wang W, Liang H, Ge X. Observation of the oil flow in a ball bearing with a novel experiment method and simulation. Tribol Int 2022;174. http://dx.doi.org/10.1016/j.triboint.2022.107731.

[13] Chen H, Liang H, Wang W, Zhang S. Investigation on the oil transfer behaviors and the air-oil interfacial flow patterns in a ball bearing under different capillary conditions. Friction 2023;11(2):228–45. http://dx.doi.org/10.1007/s40544-021-0592-3.

[14] Fan Z, Zhao Z, Liang H, Zhang Y, Wang W, Zhang S. Lubricating oil distribution in a rolling bearing using laser induced fluorescence method. Mocaxue Xuebao/Tribology 2022;42(2):234–41. http://dx.doi.org/10.16078/j.tribology.2021046.

[15] Arya U, Sadeghi F, Aamer S, Meinel A, Grillenberger H. In situ visualization and analysis of oil starvation in ball bearing cages. Tribol Trans 2023;66(5):965–78. http://dx.doi.org/10.1080/10402004.2023.2253867.

[16] Noda T, Shibasaki K, Wang Q. X-ray ct imaging of grease behavior in ball bearing and multi-scale grease flows simulation. 2016, p. 361–2,

[17] Noda T, Shibasaki K, Miyata S, Taniguchi M. X-ray CT imaging of grease behavior in ball bearing and numerical validation of multi-phase flows simulation. Tribol Online 2020;15(1):36–44. http://dx.doi.org/10.2474/trol.15.36.

[18] Fryza J, Kroupa J, Sperka P, Krupka I, Hartl M. Investigation of film thickness of grease-lubricated thrust bearing: from ball-on-disc to bearing. Proc Eng Sci 2019;1(1):550–4. http://dx.doi.org/10.24874/PES01.01.072.

[19] Manjunath M, Hausner S, Heine A, De Baets P, Fauconnier D. Electrical impedance spectroscopy for precise film thickness assessment in line contacts. Lubricants 2024;12(2). http://dx.doi.org/10.3390/lubricants12020051.

[20] Gorse P, Dullenkopf K, Bauer H-J, Wittig S. An experimental study on droplet generation in bearing chambers caused by roller bearings. In: Turbo expo: power for land, sea, and air. 43147, 2008, p. 1681–92. http://dx.doi.org/10.1115/GT2008-51281.

[21] Yan K, Dong L, Zheng J, Li B, Wang D, Sun Y. Flow performance analysis of different air supply methods for high speed and low friction ball bearing. Tribol Int 2018;121:94–107. http://dx.doi.org/10.1016/j.triboint.2018.01.035.

[22] Arya U, Peterson W, Sadeghi F, Meinel A, Grillenberger H. Investigation of oil flow in a ball bearing using bubble image velocimetry and CFD modeling. Tribol Int 2023;177:107968. http://dx.doi.org/10.1016/j.triboint.2022.107968.

[23] Ross S. Lubricant foaming and aeration study, Part I. Technical Report AFWAL-TR, Air Force Wright Aeronautical Laboratories (United States); 1984.

[24] Ross S. Lubricant foaming and aeration study, Part II. Technical Report AFWAL-TR, Air Force Wright Aeronautical Laboratories (United States); 1985, pt 2.

[25] Koczo K, Leatherman MD, Hughes K, Knobloch D. Foaming chemistry and physics. In: Lubricant additives. CRC Press; 2017, p. 337–84.

[26] Zhan C, Saint-Jalmes A, Receveur M, El Bahi H, Rondelez F, Leroy V. Detailed characterization of aeration in lubricating oils by an ultrasonic approach. Tribol Int 2022;175. http://dx.doi.org/10.1016/j.triboint.2022.107782.

[27] Duan X, Hou J, Li S, Cheng T, Yu H. Progresses and future trends in research of oil resistant foaming agent. Shiyou Huagong/Petrochemical Technol 2013;42(8):935–40.

[28] Bukvić M, Gajević S, Skulić A, Savić S, Ašonja A, Stojanović B. Tribological application of nanocomposite additives in industrial oils. Lubricants 2024;12(1). http://dx.doi.org/10.3390/lubricants12010006, Cited by: 16.

[29] Maccioni L, Chernoray V, Bohnert C, Concli F. Particle image velocimetry measurements inside a tapered roller bearing with an outer ring made of sapphire: Design and operation of an innovative test rig. Tribol Int 2022;165. http://dx.doi.org/10.1016/j.triboint.2021.107313.

[30] Maccioni L, Chernoray V, Mastrone M, Bohnert C, Concli F. Study of the impact of aeration on the lubricant behavior in a tapered roller bearing: Innovative numerical modelling and validation via particle image velocimetry. Tribol Int 2022;165. http://dx.doi.org/10.1016/j.triboint.2021.107301.

[31] Maccioni L, Chernoray VG, Concli F. Fluxes in a full-flooded lubricated tapered roller bearing: Particle image velocimetry measurements and computational fluid dynamics simulations. Tribol Int 2023;188. http://dx.doi.org/10.1016/j.triboint.2023.108824.

[32] Leibensperger R. An analysis of the flow of oil through a tapered roller bearing. J Tribol 1972;94(2):125–30. http://dx.doi.org/10.1115/1.3451652.

[33] Liebrecht J, Si X, Sauer B, Schwarze H. Investigations of hydraulic losses in in tapered roller bearings [untersuchungen von hydraulischen verlusten an kegelrollenlagern]. Tribol Schmierungstech 2015;62(3):14–21.

[34] Liebrecht J, Si X, Sauer B, Schwarze H. Investigation of drag and churning losses on tapered roller bearings. Strojniski Vestnik/J Mech Eng 2015;61(6):399–408. http://dx.doi.org/10.5545/sv-jme.2015.2490.

[35] Sedlář M, Abrahámek P. Numerical analysis of oil lubrication and cooling of roller thrust bearing in high-performance mixed-flow pump. Energies 2023;16(19). http://dx.doi.org/10.3390/en16196890.

[36] Zhu W, Zhu R, Tang X, Lu F, Bai X, Wu X, et al. CFD-based analysis of oil and gas two-phase flow characteristics in double-row tapered roller bearings with different rib structures. Appl Sci (Switzerland) 2022;12(3). http://dx.doi.org/10.3390/app12031156.

[37] OpenFOAM Foundation. Openfoam: The open source CFD toolbox. 2024, https://www.openfoam.com/ (Accessed 5 September 2024).

[38] Concli F, Schaefer C, Bohnert C. Innovative meshing strategies for bearing lubrication simulations. Lubricants 2020;8(4). http://dx.doi.org/10.3390/LUBRICANTS8040046.

[39] Majdoub F, Mevel B. Kinematic equilibrium of rollers in tapered roller bearings. Tribol Trans 2019.

[40] Yakhot V, Orszag SA, Thangam S, Gatski T, Speziale C. Development of turbulence models for shear flows by a double expansion technique. Phys Fluids 1992;4(7):1510–20.

[41] Souders DT, Hirt C. Modeling entrainment of air at turbulent free surfaces. 2004, p. 1344–52, URL https://www.scopus.com/inward/record.uri?eid=2-s2.0-23844507576&partnerID=40&md5=5b936ce601551e9a55bc709b8feb4981.

[42] Mastrone M, Concli F. Numerical modeling of fluid's aeration: Analysis of the power losses and lubricant distribution in gearboxes. J Appl Comput Mechanics 2023;9(1):83–94. http://dx.doi.org/10.22055/jacm.2022.40666.3625.

[43] Lopes P, Leandro J, Carvalho RF. Self-aeration modelling using a sub-grid volume-of-fluid model. Int J Nonlinear Sci Numer Simul 2017;18(7–8):559–74. http://dx.doi.org/10.1515/ijnsns-2017-0015, [cited 2024-07-12].

[44] Maccioni L, Rüth L, Koch O, Concli F. Load-independent power losses of fully flooded lubricated tapered roller bearings: Numerical and experimental investigation of the effect of operating temperature and housing wall distances. Tribol Trans 2023;66(6):1078–94. http://dx.doi.org/10.1080/10402004.2023.2254957.